GEOPHYSICS, VOL. 82, NO. 5 (SEPTEMBER-OCTOBER 2017); P. S377–S389, 20 FIGS., 1 TABLE.
10.1190/GEO2016-0565.1

Check for updates

Downloaded 10/27/17 to 138.67.129.100. Redistribution subject to SEG license or copyright; see Terms of Use at http://library.seg.org/

3D angle decomposition for elastic reverse time migration

Yuting Duan[1] and Paul Sava[1]

ABSTRACT

We have developed three approaches for 3D angle decomposition using elastic reverse time migration. The first approach uses time- and space-lag common-image point gathers computed from elastic wavefields. This method facilitates computing angle gathers at sparse and possibly irregularly distributed points in the image. The second approach transforms extended time-lag images to the angle domain using slant stacks along 4D surfaces, instead of using slant stacks along 2D straight lines. The third approach transforms space-lag common-image gathers to the angle domain. The three proposed methods solve a system of equations that handles dipping reflectors, and they yield angle gathers that are more accurate compared with those obtained via alternative existing methods. We have developed our methods using 2D and 3D synthetic and field data examples and found that they provide accurate opening and azimuth angles and they can handle steeply dipping reflectors and converted wave modes.

INTRODUCTION

Common reflection-angle gathers are important tools for migration velocity analysis and amplitude-versus-angle analysis. In areas with complex geologic structures such as salt bodies, severe wavefield distortions lead to irregular subsurface illumination patterns, even if the acquisition distribution is uniform. Angle gathers can provide indication of subsalt illumination, which benefits reservoir characterization and acquisition design. Angle-decomposition techniques can be classified into two categories, depending on the type of migration used: ray-based methods and wavefield-based methods. Ray-based methods (Brandsberg-Dahl et al., 1999; Audebert et al., 2000; Xu et al., 2001) are convenient because they are straightforward and efficient for obtaining angle information from raypaths traced to an image point. However, the accuracy of ray-based algorithms suffers in areas where velocity contrast is strong, for example, in the presence of salt bodies. Wavefield-based angle-decomposition methods rely on decomposition of the wavefield into plane-wave components (De Bruin et al., 1990; Xie and Wu, 2002; Sava and Fomel, 2003; Biondi and Symes, 2004; Yoon et al., 2004; Sava, 2007; Sava and Vlad, 2011; Xu et al., 2011). Although they are more computationally expensive than ray-based methods, wavefield-based methods are superior because they accurately simulate wave propagation in complex geologic structures.

Wavefield-based methods generally fall into two categories: preimaging and postimaging algorithms (Vyas et al., 2011). Preimaging methods include techniques that decompose the wavefields prior to the imaging condition, for example, by f-k domain decomposition (Xu et al., 2011), or by Poynting vector methods (Yoon and Marfurt, 2006; Yan and Ross, 2013). Because f-k domain decomposition requires 4D Fourier transforms in 3D models, the computational cost can be high. Poynting vector methods are less computationally intensive but may yield inaccurate angle information when wavefields are complicated, e.g., by triplicated wavefronts (Patrikeeva and Sava, 2013). Postimaging methods, which decompose migrated images to angle gathers after application of an imaging condition, typically require two steps: computation of extended images as a function of space- or time-lag gathers followed by mapping of the images from the extended domain to the angle domain. The extended images can be space-lag common-image gathers (λCIGs) (Rickett and Sava, 2002; Sava and Fomel, 2003), time-lag common-image gathers (τCIGs) (Sava and Fomel, 2006), or mixed time- and space-lag common-image point (CIP) gathers (Sava and Vlad, 2011). Angle gathers computed using λCIGs or τCIGs describe the reflectivity as a function of a space axis (typically the depth axis), whereas for CIPs, the angle-dependent reflectivity is evaluated at selected points in the subsurface.

Wavefield-based angle-decomposition methods can be extended to elastic media. Algorithms for elastic wavefield-based angle decomposition have also been proposed (Yan and Sava, 2008; Frigerio and Sava, 2011; Yan and Xie, 2012). One important aspect of angle

Manuscript received by the Editor 4 November 2016; revised manuscript received 19 April 2017; published ahead of production 26 May 2017; published online 16 August 2017.
[1]Center for Wave Phenomena, Colorado School of Mines, Golden, Colorado, USA. E-mail: yduan@mines.edu; psava@mines.edu.
© 2017 Society of Exploration Geophysicists. All rights reserved.

Downloaded 10/27/17 to 138.67.129.100. Redistribution subject to SEG license or copyright; see Terms of Use at http://library.seg.org/

decomposition using elastic wavefields is the choice of imaging condition that separates the different wave modes. Yan and Sava (2008) propose an extended imaging condition that crosscorrelates pure P- and S-wavefields from the source and receiver. The amplitudes of computed CIGs for different types of reflections (PP, PS, SP, and SS) are related to their reflection coefficients, and these CIGs can be mapped to the angle domain through a process similar to that used in the acoustic case. However, the shear wavefield after Helmholtz decomposition has three nonzero components in 3D, which makes it challenging to include information from all components in PS angle gathers. Moreover, because PS and SP reflectivities reverse sign at normal incidence in isotropic media (Balch and Erdemir, 1994), PS and SP images without corrections may destructively interfere when stacked over the experiments of a seismic survey. Duan and Sava (2015b) propose a scalar imaging condition for converted waves that yields 3D PS and SP scalar images without polarity reversal. We extend this imaging condition to compute scalar PS and SP extended images from elastic wavefields, which can then be used for 3D angle decomposition.

In this paper, we present improved methods for opening and azimuth angle decomposition for elastic reverse time migration (RTM). We develop an extended scalar imaging condition from the zero-lag scalar imaging condition introduced by Yan and Sava (2008). Our methods use local plane-wave decompositions of extended images and exploit the relationships among the time-lag, space-lag, and image shift in space. These relationships lead to opening and azimuth angle decomposition for PP, PS, SP, and SS reflections using either time-lag CIG (τ), space-lag CIG (λ), or time- and space-lag CIP gathers.

ELASTIC SCALAR IMAGING CONDITION

Duan and Sava (2015b) develop a scalar imaging condition using geometric relationships between the P- and S-wave propagation directions, the reflector orientation, and the S-wave polarization direction. The PS and SP images computed using this imaging condition are scalars without polarity reversal. Combining this scalar imaging condition for converted waves with the conventional PP and SS imaging conditions (Etgen, 1988; Yan and Sava, 2008), we obtain an elastic imaging condition defined by the following equations for PP, PS, SP, and SS reflectivity:

$$I^{\mathrm{PP}}(\mathbf{x}) = \sum_{e,t} P_s(e,\mathbf{x},t) P_r(e,\mathbf{x},t), \tag{1}$$

$$I^{\mathrm{PS}}(\mathbf{x}) = \sum_{e,t} [\nabla P_s(e,\mathbf{x},t) \times \mathbf{n}(\mathbf{x})] \cdot \mathbf{S}_r(e,\mathbf{x},t), \tag{2}$$

$$I^{\mathrm{SP}}(\mathbf{x}) = \sum_{e,t} [(\nabla \times \mathbf{S}_s(e,\mathbf{x},t)) \cdot \mathbf{n}(\mathbf{x})] P_r(e,\mathbf{x},t), \tag{3}$$

$$I^{\mathrm{SS}}(\mathbf{x}) = \sum_{e,t} \mathbf{S}_s(e,\mathbf{x},t) \cdot \mathbf{S}_r(e,\mathbf{x},t). \tag{4}$$

The vector $\mathbf{n}(\mathbf{x})$ represents the normal to the reflector plane. Duan and Sava (2015a) suggest estimating reflector normals from stacked PS and SP images computed using a conventional imaging method, which is applicable even when the reflectors are imaged at incorrect positions due to velocity errors. Quantities $P(e,\mathbf{x},t)$ and $\mathbf{S}(e,\mathbf{x},t)$ represent P and S wavefields obtained by wave-mode separation, as functions of experiment e, time t, and space $\mathbf{x}$. Subscripts s and r denote source- and receiver-side wavefields, respectively. Scalar P- and vector S-wavefields are computed from displacement wavefields using Helmholtz decomposition (Dellinger and Etgen, 1990; Yan and Sava, 2008):

$$P(e,\mathbf{x},t) = \nabla \cdot \mathbf{u}(e,\mathbf{x},t), \tag{5}$$

$$\mathbf{S}(e,\mathbf{x},t) = \nabla \times \mathbf{u}(e,\mathbf{x},t). \tag{6}$$

An extended imaging condition defines the image as a function of space and crosscorrelation lags, i.e., space-lag $\boldsymbol{\lambda}$ and time-lag τ:

$$I^{\mathrm{PP}}(\mathbf{x},\boldsymbol{\lambda},\tau) = \sum_{e,t} P_s(\mathbf{x}-\boldsymbol{\lambda},t-\tau) P_r(\mathbf{x}+\boldsymbol{\lambda},t+\tau), \tag{7}$$

$$I^{\mathrm{PS}}(\mathbf{x},\boldsymbol{\lambda},\tau) = \sum_{e,t} [\nabla P_s(\mathbf{x}-\boldsymbol{\lambda},t-\tau) \times \mathbf{n}(\mathbf{x})] \cdot \mathbf{S}_r(\mathbf{x}+\boldsymbol{\lambda},t+\tau), \tag{8}$$

$$I^{\mathrm{SP}}(\mathbf{x},\boldsymbol{\lambda},\tau) = \sum_{e,t} [\nabla \times \mathbf{S}_s(\mathbf{x}-\boldsymbol{\lambda},t-\tau) \cdot \mathbf{n}(\mathbf{x})] P_r(\mathbf{x}+\boldsymbol{\lambda},t+\tau), \tag{9}$$

$$I^{\mathrm{SS}}(\mathbf{x},\boldsymbol{\lambda},\tau) = \sum_{e,t} \mathbf{S}_s(\mathbf{x}-\boldsymbol{\lambda},t-\tau) \cdot \mathbf{S}_r(\mathbf{x}+\boldsymbol{\lambda},t+\tau). \tag{10}$$

The quantities $\boldsymbol{\lambda} = (\lambda_x, \lambda_y, \lambda_z)$ and τ describe the space shift and time shift, respectively, between the source and receiver wavefields prior to imaging.

Such extended images can be used for, for example, tomographic velocity analysis (Symes, 1993; Sava and Biondi, 2004; Yang and Sava, 2015) and migration artifact attenuation (Zhang and Sun, 2008; Duan and Sava, 2014). The extended images also contain the moveout information that can be used for angle decomposition, as we illustrate in the following section.

MOVEOUT ANALYSIS

The extended imaging condition in equations 7–10 preserves the information necessary for decomposing images into angle-dependent components. In 3D, the PP, PS, SP, and SS images obtained using this imaging condition are scalars at each spatial location, and they can be used to directly compute angle gathers. We formulate our method under the assumption that reflectors, as well as incident and reflected wavefields, are locally planar. However, the derived algorithms are not limited to cases in which the wavefronts are planar because waves can always be decomposed into their planar components, even in complex wavefields with triplicated waves.

Downloaded 10/27/17 to 138.67.129.100. Redistribution subject to SEG license or copyright; see Terms of Use at http://library.seg.org/

We define the angle domain with half-opening angle θ and azimuth ϕ, and we use the following unit vectors to describe the angle-decomposition procedure (Figure 1):

- **o**: azimuth vector acting as a reference direction, e.g., north
- **n**: reflector normal
- **a**: projection of the azimuth vector onto the interface plane

$$\mathbf{a} = (\mathbf{n} \times \mathbf{o}) \times \mathbf{n} \tag{11}$$

- $\mathbf{n}_s$: propagation direction of the incident wave
- $\mathbf{n}_r$: propagation direction of the reflected wave
- **q**: vector lying at the intersection of the interface and the reflection plane

$$\mathbf{q} = Q(\mathbf{n}, \phi)\mathbf{a}, \tag{12}$$

where $Q(\mathbf{n}, \phi)$ is a rotation matrix defined by the axis **n** and the angle ϕ

$$Q = \begin{bmatrix} n_x^2+(n_y^2+n_z^2)c & n_x n_y(1-c)-n_z s & n_x n_z(1-c)+n_y s \\ n_y n_x(1-c)+n_z s & n_y^2+(n_z^2+n_x^2)c & n_y n_z(1-c)-n_x s \\ n_z n_x(1-c)-n_y s & n_z n_y(1-c)+n_x s & n_z^2+(n_x^2+n_y^2)c \end{bmatrix}, \tag{13}$$

where quantities $s = \sin\phi$ and $c = \cos\phi$.

The (locally planar) source-wavefield propagates along the direction indicated by vector $\mathbf{n}_s$ with speed v_s, and the (locally planar) receiver-wavefield propagates along the direction indicated by vector $\mathbf{n}_r$ with speed v_r. As shown in Figure 2a, the vector $\mathbf{x}_o$ indicates a point at the intersection of the two wavefronts and the reflection plane at time $t = t_o$:

$$\begin{cases} \mathbf{n}_s \cdot (\mathbf{x} - \mathbf{x}_o) = v_s(t - t_o), & (14) \\ \mathbf{n}_r \cdot (\mathbf{x} - \mathbf{x}_o) = v_r(t - t_o). & (15) \end{cases}$$

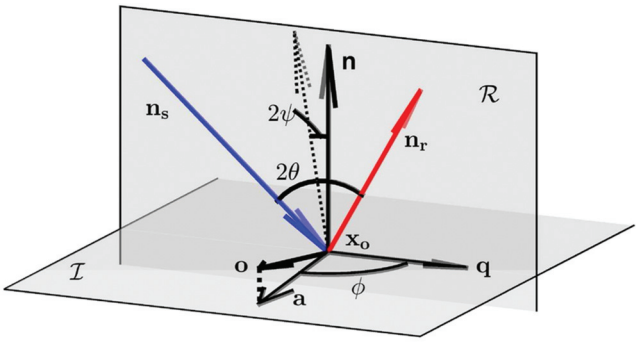


Figure 1. Schematic representation of the angles and vectors used in opening and azimuth angle decomposition for an image point $\mathbf{x}_o$. The $\mathcal{I}$ and $\mathcal{R}$ are the interface and reflection planes, respectively. Vector **n** indicates the normal to the interface $\mathcal{I}$, vector $\mathbf{n}_s$ defines the propagation direction of the incident wave, vector $\mathbf{n}_r$ defines the propagation direction of the reflected wave, vector **a** is the projection of the azimuth vector in the interface plane, vector **o** is the reference direction, and vector **q** lies at the intersection of the interface and reflection planes. The opening angle 2θ is the sum of the incidence and reflection angles. The dashed arrow is the bisector of the opening angle. Angle 2ψ is their difference, and angle ϕ is the azimuth.

Introducing space-lag $\boldsymbol{\lambda}$ to equations 14 and 15 is equivalent to shifting the wavefronts in space, and introducing time-lag τ is equivalent to propagating the wavefronts in time. For equation 14, we shift the source wavefront in space by $+\boldsymbol{\lambda}$. At time $t = t_o - \tau$, the source wavefront is described by

$$\mathbf{n}_s \cdot (\mathbf{x} - \mathbf{x}_o - \boldsymbol{\lambda}) = v_s(-\tau). \tag{16}$$

For equation 15, we shift the receiver wavefront in space by $-\boldsymbol{\lambda}$. At time $t = t_o + \tau$, the receiver wavefront is described by

$$\mathbf{n}_r \cdot (\mathbf{x} - \mathbf{x}_o + \boldsymbol{\lambda}) = v_r(+\tau). \tag{17}$$

The intersection of the two wavefronts in the reflection plane is shifted to position **x**, outside the local reflector plane as shown in Figure 2b. The expressions relating the extended images using the locally planar source and receiver wavefields are

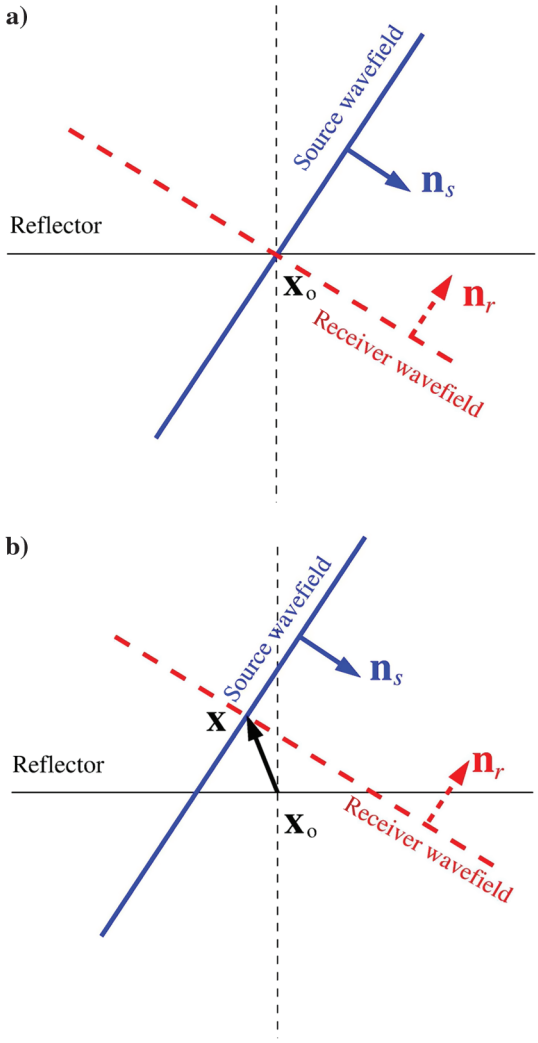


Figure 2. Cartoon describing source and receiver planes intersecting in the reflection plane (a) at location $\mathbf{x}_o$ at time t_o, and (b) at location **x** after moving planes along time- and space-axes. Vectors $\mathbf{n}_s$ and $\mathbf{n}_r$ define the propagation directions of the incident and reflected waves in space, respectively.

$$\begin{cases} \left(\frac{\mathbf{n}_s}{v_s}-\frac{\mathbf{n}_r}{v_r}\right)\cdot(\mathbf{x}-\mathbf{x}_o)-\left(\frac{\mathbf{n}_s}{v_s}+\frac{\mathbf{n}_r}{v_r}\right)\cdot\boldsymbol{\lambda}=-2\tau, & (18)\\ \left(\frac{\mathbf{n}_s}{v_s}+\frac{\mathbf{n}_r}{v_r}\right)\cdot(\mathbf{x}-\mathbf{x}_o)-\left(\frac{\mathbf{n}_s}{v_s}-\frac{\mathbf{n}_r}{v_r}\right)\cdot\boldsymbol{\lambda}=0, & (19)\end{cases}$$

which are obtained by the sum and difference of equations 16 and 17. The vector $(\mathbf{x}-\mathbf{x}_o)$ measures the spatial shift of the image point, corresponding to time-lag τ and space-lag $\boldsymbol{\lambda}$. We replace vectors $\mathbf{n}_s$ and $\mathbf{n}_r$ with functions of vectors $\mathbf{n}$ and $\mathbf{q}$:

$$\begin{cases} \mathbf{n}_s=\mathbf{q}\,\sin(\theta-\psi)-\mathbf{n}\,\cos(\theta-\psi), & (20)\\ \mathbf{n}_r=\mathbf{q}\,\sin(\theta+\psi)+\mathbf{n}\,\cos(\theta+\psi). & (21)\end{cases}$$

As shown in Figure 1, the angle 2θ is the sum of the incidence and reflection angles, and the angle 2ψ is their difference. Thus, the incidence angle is $\theta-\psi$, and the reflection angle is $\theta+\psi$. With γ as the ratio of the source-side wave speed v_s and receiver-side wave speed v_r, we use Snell's law to obtain the expression

$$\gamma=\frac{v_s}{v_r}=\frac{\sin(\theta-\psi)}{\sin(\theta+\psi)}, \qquad (22)$$

as well as the following relation among ψ, γ, and θ:

$$\tan\psi=\frac{1-\gamma}{1+\gamma}\tan\theta. \qquad (23)$$

By substituting equation 23 in equations 20 and 21, we can replace the angle ψ with a function of γ and θ:

$$\begin{cases} \mathbf{n}_s+\gamma\mathbf{n}_r=\frac{[(\gamma^2-1)\mathbf{n}+2\mathbf{q}\gamma\,\sin 2\theta]}{\sqrt{\gamma^2+1+2\gamma\,\cos 2\theta}}, & (24)\\ \mathbf{n}_s-\gamma\mathbf{n}_r=-\mathbf{n}\sqrt{\gamma^2+1+2\gamma\,\cos 2\theta}, & (25)\end{cases}$$

Algorithm 1. Isotropic angle decomposition using extended image.

```
1) for each CIP do
2)    input I(x, λ, τ)
3)    input n, o, γ, v_s
4)    {n, o} → a
5)    for φ = 0°...360° do
6)       {n, a, φ} → q
7)       for θ = 0°...90° do
8)          I(x, λ, τ) ⇒ I(φ, θ)
9)       end for
10)   end for
11)   return I(φ, θ)
12) end for
```

which can be substituted in equations 18 and 19 to form a system of equations for angle decomposition.

ANGLE-DECOMPOSITION METHODS

Pseudocode for angle decomposition using the extended image $\mathbf{I}(\mathbf{x},\boldsymbol{\lambda},\tau)$ is provided in Algorithm 1 (Sava and Vlad, 2011). Given the normal vector $\mathbf{n}$ and the azimuth reference vector $\mathbf{o}$, we first compute vector $\mathbf{a}$, which is the projection of the azimuth vector onto the interface plane. Then, we loop over all possible values of the azimuth angle ϕ and construct the vector $\mathbf{q}$, which lies at the intersection of the interface and reflection planes. This step is a rotation of the azimuth reference vector $\mathbf{a}$ within the interface plane by the azimuth angle ϕ. Next, we loop over all possible values of the reflection angle θ and apply a slant stack to the extended image $\mathbf{I}(\mathbf{x},\boldsymbol{\lambda},\tau)$ to obtain the output image $\mathbf{I}(\phi,\theta)$ as a function of half-opening angle θ and azimuth angle ϕ.

The system of equations we use for angle decomposition (equations 18 and 19) describes the relationships among the three quantities, time-lag τ, space-lag $\boldsymbol{\lambda}$, and image shift $(\mathbf{x}-\mathbf{x}_o)$. And we consider three special cases of this system by zeroing one of the quantities, which leads to angle-decomposition methods using different types of extended images: space- and time-lag, time-lag only, and space-lag only. For each type of extended image, we derive the equations that connect extended images with wide-azimuth angle gathers.

Time- and space-lag CIP gather

For time- and space-lag CIP gathers, we derive the relationships between time- and space-lags at point $\mathbf{x}_o$ from equations 18 and 19 by setting $\mathbf{x}=\mathbf{x}_o$:

$$\begin{cases} \left(\frac{\mathbf{n}_s}{v_s}+\frac{\mathbf{n}_r}{v_r}\right)\cdot\boldsymbol{\lambda}=2\tau, & (26)\\ \left(\frac{\mathbf{n}_s}{v_s}-\frac{\mathbf{n}_r}{v_r}\right)\cdot\boldsymbol{\lambda}=0. & (27)\end{cases}$$

Substituting equations 24 and 25 in equations 26 and 27, we obtain the system of equations that describes the relationships between space-lag $\boldsymbol{\lambda}$ and time-lag τ:

$$\begin{cases} \frac{\gamma\,\sin 2\theta}{\sqrt{\gamma^2+1+2\gamma\,\cos 2\theta}}(\mathbf{q}\cdot\boldsymbol{\lambda})=v_s\tau, & (28)\\ \mathbf{n}\cdot\boldsymbol{\lambda}=0. & (29)\end{cases}$$

We see that, from equation 29, only space-lags that are orthogonal to the reflector normal vector $\mathbf{n}$ contribute to the extended image.

Equations 28 and 29 simplify for PP reflections, for which velocity ratio $\gamma=1$ (Sava and Fomel, 2003):

$$\begin{cases} \sin\theta(\mathbf{q}\cdot\boldsymbol{\lambda})=v_s\tau, & (30)\\ \mathbf{n}\cdot\boldsymbol{\lambda}=0. & (31)\end{cases}$$

Similar to equation 28, equation 30 describes a linear relationship between space-lag $\boldsymbol{\lambda}$ and time-lag τ.

We illustrate this angle-decomposition method using a 3D model with a horizontal reflector at depth $z=0.2$ km, shown in Figure 3.

Downloaded 10/27/17 to 138.67.129.100. Redistribution subject to SEG license or copyright; see Terms of Use at http://library.seg.org/

Downloaded 10/27/17 to 138.67.129.100. Redistribution subject to SEG license or copyright; see Terms of Use at http://library.seg.org/

The P-wave velocities of the first and second layers are 2.5 and 3.0 km/s, respectively. The S-wave velocity model is constant (1.5 km/s). The acquisition geometry consists of a 2D network of receivers at $z = 0.02$ km. We generate a 3C shot gather using a vertical displacement source at coordinates (0.4, 0.4, 0.02) km with a 110 Hz peak frequency Ricker wavelet. Figure 4a and 4b shows the PP and PS images, respectively, which are computed using the imaging condition shown in equations 1 and 2. Notice that additional events in the PP and PS images are artifacts, and they are generated by nonphysical modes in the constructed receiver wavefield (Duan and Sava, 2014). The PP and PS images are scalars without polarity reversal. Figure 5a shows a PP CIP gather of an image point at coordinates (0.33, 0.33, 0.2) km. Using Algorithm 1, we compute the angle gather shown in the top right panel of Figure 5a. The dot overlain on the angle gather indicates the analytical solution of the opening and azimuth angle for the given acquisition geometry. We also compute PP angle gathers for eight different shots, shown in Figure 5b. Because the migration velocity is correct, the summation of the eight extended PP images yields a focused point at $\tau = 0, \boldsymbol{\lambda} = \mathbf{0}$. The top right panel of Figure 5b shows the combination of eight PP angle gathers at the center of the reflector, which match the analytical solution shown as dots. Similarly, we compute the PS angle gather from the CIP gather (Figure 6a) at coordinates (0.2, 0.2, 0.2) km. The computed PP and PS angle gathers match the analytical results, which demonstrates the accuracy of the angle-decomposition algorithm.

Time-lag CIG

For time-lag CIG (τ), we set $\boldsymbol{\lambda} = \mathbf{0}$ in equations 18 and 19 to obtain

$$\begin{cases} \left(\dfrac{\mathbf{n}_s}{v_s} - \dfrac{\mathbf{n}_r}{v_r}\right) \cdot (\mathbf{x} - \mathbf{x}_o) + 2\tau = 0, & (32) \\ \left(\dfrac{\mathbf{n}_s}{v_s} + \dfrac{\mathbf{n}_r}{v_r}\right) \cdot (\mathbf{x} - \mathbf{x}_o) = 0. & (33) \end{cases}$$

This system of equations shows the relationships between image shift $(\mathbf{x} - \mathbf{x}_o)$ and time-lag τ.

Substituting equations 24 and 25 in equations 32 and 33, we obtain the system for angle decomposition using time-lag extended images:

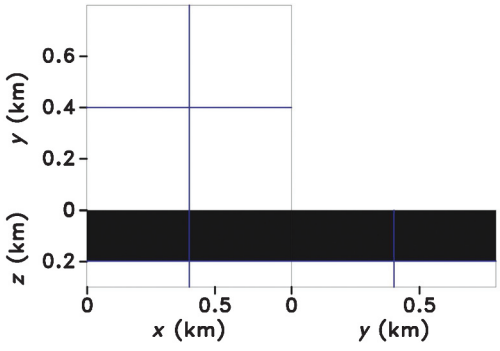


Figure 3. The 3D P-velocity model with one horizontal reflector at $z = 0.2$ km in a homogeneous medium. The acquisition geometry consists of a vertical displacement source at (0.4, 0.4, 0.02) km and a 2D network of receivers at $z = 0.02$ km.

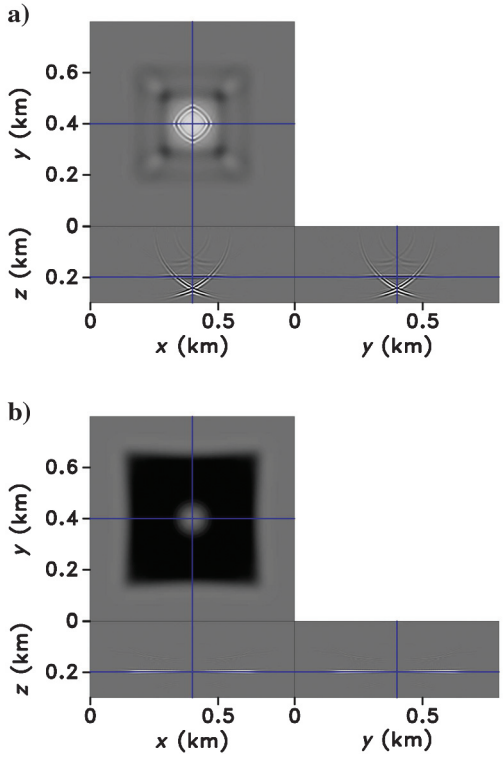


Figure 4. (a) The PP and (b) PS images computed for one shot at (0.4, 0.4, 0.02) km. The horizontal reflector is at $z = 0.2$ km.

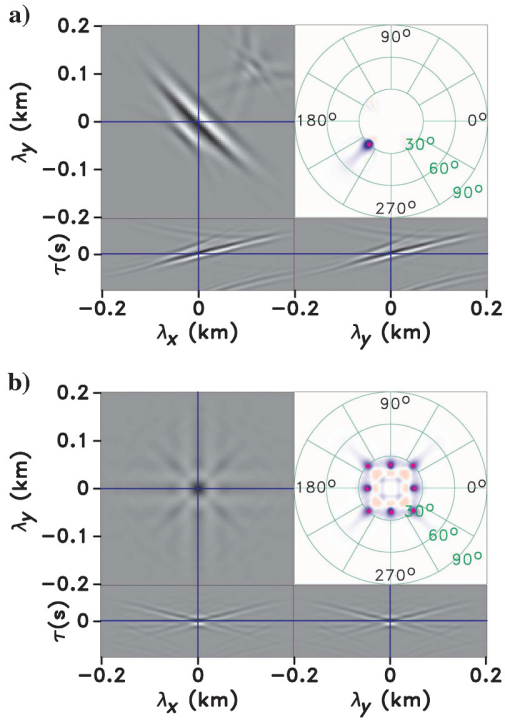


Figure 5. The PP extended CIP and wide-azimuth angle gathers of (a) a picked image point at coordinates (0.33, 0.33, 0.2) km for one shot at coordinates (0.4, 0.4, 0.02) km and (b) a picked image point at coordinates (0.4, 0.4, 0.2) km for eight shots. The red dots represent the analytical solution of the opening and azimuth angles using the acquisition geometry.

$$\begin{cases} \frac{\sqrt{\gamma^2+1+2\gamma\cos 2\theta}}{2}[\mathbf{n}\cdot(\mathbf{x}-\mathbf{x}_o)] = v_s\tau, & (34) \\ \sin 2\theta\sqrt{\gamma^2+1+2\gamma\cos 2\theta}[\mathbf{q}\cdot(\mathbf{x}-\mathbf{x}_o)] = v_s\tau\left(\frac{1}{\gamma}-\gamma\right), & (35) \end{cases}$$

where equation 34 corresponds to the projection of the image shift $(\mathbf{x}-\mathbf{x}_o)$ onto the reflector normal $\mathbf{n}$, and equation 35 corresponds to the projection of the image shift $(\mathbf{x}-\mathbf{x}_o)$ onto vector $\mathbf{q}$.

In the acoustic case in which velocity ratio $\gamma = 1$, equations 34 and 35 simplify to (Sava and Fomel, 2006)

$$\begin{cases} \cos\theta[\mathbf{n}\cdot(\mathbf{x}-\mathbf{x}_o)] = v_s\tau, & (36) \\ \mathbf{q}\cdot(\mathbf{x}-\mathbf{x}_o) = 0. & (37) \end{cases}$$

Note that in equation 37, the time-lag τ is not related to the azimuth vector $\mathbf{q}$, i.e., time-lag extended images do not contain azimuthal information for the acoustic case; however, for converted waves for which $\gamma \neq 1$, time-lag extended images contain azimuthal information, according to equation 35.

We compute a 3D PS angle gather for the simple 3D model with one flat reflector (Figure 3) using the time-lag CIG method. Figure 7 shows the τCIG at $x = 0.2$ km and the wide-azimuth angle gather for the image point at coordinates (0.2, 0.2, 0.2) km. The red dot represents the analytical solution of the opening and azimuth angle using the acquisition geometry. The resolution of the azimuth angle is low because it depends on how close the velocity ratio γ is to one (here, $\gamma = 1.67$). Although the resolution of the azimuth angle gathers for converted waves depends on the velocity ratio γ, the possibility of obtaining the azimuthal information from the time-lag gathers is attractive because computing time-lag gathers is computationally cheaper than computing space-lag gathers.

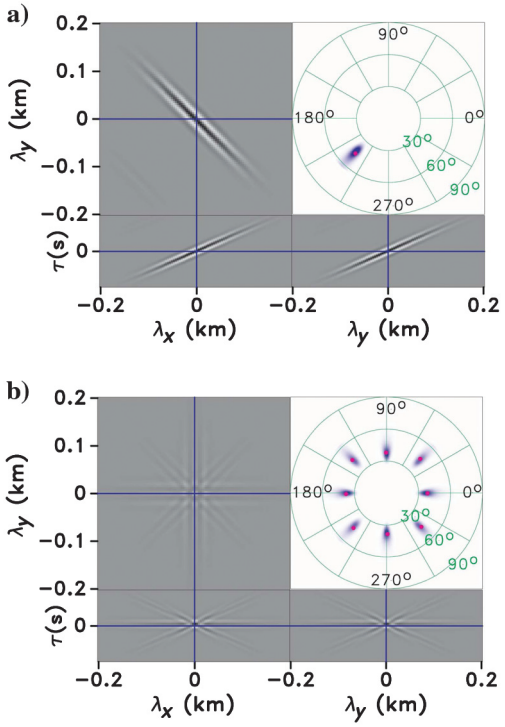


Figure 6. The PS extended CIP and wide-azimuth angle gathers of (a) a picked image point at coordinates (0.2, 0.2, 0.2) km for one shot at coordinates (0.4, 0.4, 0.02) km and (b) a picked image point at coordinates (0.4, 0.4, 0.2) km for eight shots. The red dots represent the analytical solution of the opening and azimuth angles using the acquisition geometry.

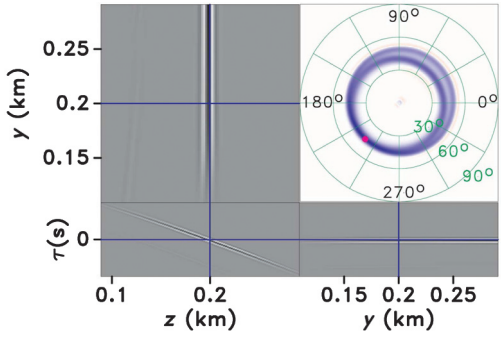


Figure 7. The PS extended τCIG at $x = 0.2$ km and the wide-azimuth angle gather of a picked image point at coordinates (0.2, 0.2, 0.2) km for the 3D model shown in Figure 3. The red dot represents the analytical solution of the opening and azimuth angle using the acquisition geometry. The energy focuses around the correct half-opening angle, but the resolution of the azimuth angle is low.

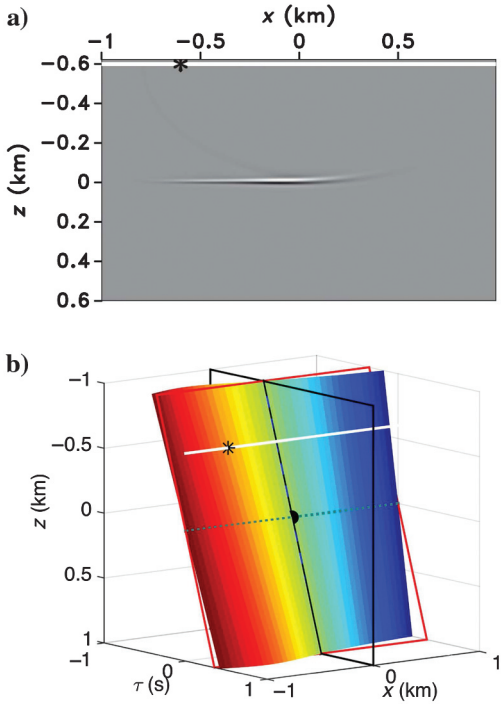


Figure 8. (a) The PP image computed from one shot gather. The reflector is horizontal at $z = 0.0$ km. The star represents the source location, and the white line represents the receiver locations. (b) Predicted spatial shift of a horizontal reflector for $\gamma = 1$. The star at coordinates $x = -0.6$ km, $z = -0.6$ km, and $\tau = 0$ s represents the source location, and the white line at $z = -0.6$ km and $\tau = 0$ s represents the receiver locations. The dotted line at $z = 0.0$ km and $\tau = 0$ s shows the zero-lag image. The line at $x = 0.0$ km illustrates the spatial shift for the image point at (0.0, 0.0) km. The colors on the surface indicate the contour of the spatial shifts for different image points.

Downloaded 10/27/17 to 138.67.129.100. Redistribution subject to SEG license or copyright; see Terms of Use at http://library.seg.org/

Downloaded 10/27/17 to 138.67.129.100. Redistribution subject to SEG license or copyright; see Terms of Use at http://library.seg.org/

If we assume that reflectors are horizontal, then equations 36 and 37 simplify to

$$\cos\,\theta(z - z_o) = v_s\tau, \tag{38}$$

which is widely used in practice due to its simplicity. The equation shows the linear relationship between depth shift and time lag. To compute angle gathers, we apply a slant stack along the vertical direction. This approach, however, is correct only if the reflectors are horizontal.

We illustrate this method with 2D examples. Figure 8a shows a PP image for a two-layered model with a horizontal reflector in the P-velocity model. The acquisition geometry consists of one source at $(-0.6, -0.6)$ km and one receiver line at $z = -0.6$ km. Using equations 36 and 37, we can predict the spatial shift of the reflector as function of time lag τ and space $\mathbf{x}$, as shown in Figure 8b. The red frame indicates the plane described in equation 36. The black line is the intersection of the plane indicated by the red frame and the vertical plane indicated by the black frame, and it shows how the image point (black dot) moves with the time lag. Because the opening angle for each image point on the reflector changes with its relative position to the source, the spatial shift for each image point also varies. Figure 9a shows the vertical CIGs at several locations, indicated by the number below each image panel. Theoretically, the shapes of the extended images in each panel are straight lines, which match the corresponding vertical slice of the surface in Figure 8b. We compare the angle gathers computed using a conventional method (Sava and Fomel, 2006) and our proposed method. The conventional method maps the time-lag gather for each vertical trace in the model domain individually to an angle gather (Figure 9b), whereas the proposed method computes angle gathers (Figure 9c) via a slant-stack along the surface shown in Figure 8b. In this example, the image shifts vertically in the time-lag gather, and the two methods produce similar results.

Figure 10a shows a PP image for a model with a dipping reflector in the P velocity. Using equations 36 and 37, we can predict the spatial shift of the reflector as a function of time-lag τ, as shown in Figure 10b. The dashed line is the intersection of the plane in-

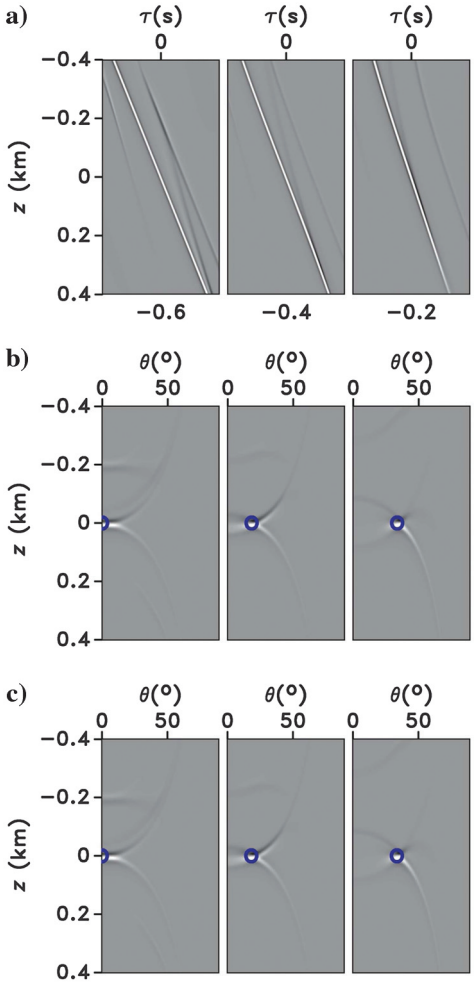


Figure 9. (a) Computed extended image gathers at several x-locations, indicated by the number below each image. The shape of the image in each panel matches the corresponding vertical slice of the surface plot in Figure 8b. Computed angles for all samples on the reflector by applying (b) a slant stack along the vertical trace, and (c) the method described in Algorithm 1, which applies a slant stack along the surface shown in Figure 8b. The circles represent the analytical solution of the opening angles using the acquisition geometry. The two methods generate the same angle gathers, and they are the same for PP reflections with flat reflectors.

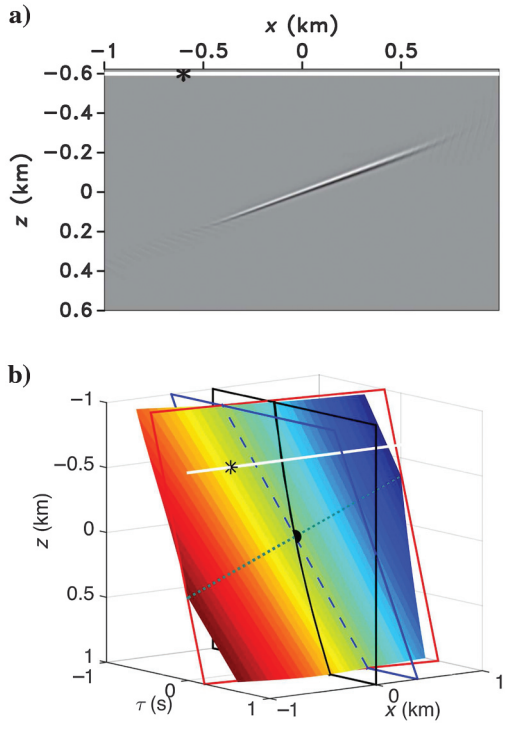


Figure 10. (a) The PP image computed from one shot gather. The reflector is dipping. (b) Predicted spatial shift of a dipping reflector for $\gamma = 1$. The star at coordinates $x = -0.6$ km, $z = -0.6$ km, and $\tau = 0$ s represents the source location, and the white line at $z = -0.6$ km and $\tau = 0$ s represents the receiver locations. The dotted line at $\tau = 0$ s shows the zero-lag image. The dashed line illustrates the spatial shift for image point at $(0.0, -0.6)$ km. The solid line at $x = 0.0$ km illustrates the extended image for a time-lag gather at a fixed horizontal position. Note that these two lines do not overlay. The colors on the surface indicate the contour of the spatial shifts for different image points.

Downloaded 10/27/17 to 138.67.129.100. Redistribution subject to SEG license or copyright; see Terms of Use at http://library.seg.org/

dicated by the red frame (equation 27) and the plane indicated by the blue frame (equation 37), which illustrates the spatial shift for the image point at $x = 0.0$ km and $z = 0.0$ km. The solid line through the image point represents the analytical moveout of the extended image in a vertical CIG. The dashed and solid lines do not coincide with each other; i.e., the method that applies a slant stack to a CIG at a fixed location in space does not accurately measure the image shift $(\mathbf{x} - \mathbf{x}_o)$. The angle gathers computed using this method and the method using a slant-stack along the surface are shown in Figure 11b and 11c, respectively. The surface slant stack leads to better focused angle gathers that have significantly higher resolution.

For converted waves, the image shifts not only vertically, but also horizontally in the time-lag gather, even for a horizontal reflector.

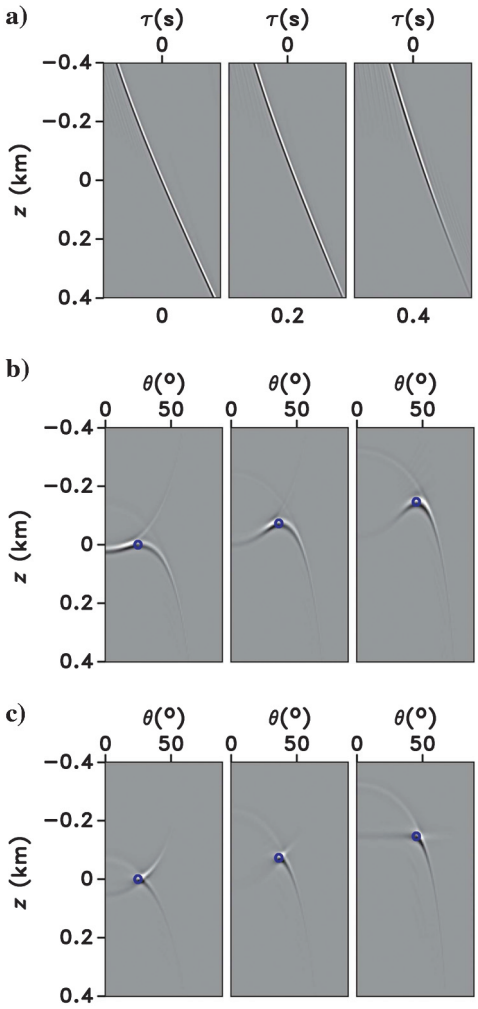


Figure 11. (a) Computed extended image gathers at several x-locations, indicated by the number below each image. The shape of the image in each panel matches the corresponding vertical slice of the surface plot in Figure 10b. Computed angles for all samples on the reflector by applying (b) a slant stack along the vertical trace and (c) the method described in Algorithm 1, which applies a slant stack along the surface shown in Figure 10b. The circles represent the analytical solution of the opening angle using the acquisition geometry. The angle gathers in (c) are more focused and accurate than those in (b).

Figure 12a shows the PS image for a two-layered model with a horizontal reflector defined by a P-velocity contrast. The predicted spatial shift of the reflector is shown in Figure 12b. The red frame indicates the plane used in equation 34, and the blue frame indicates the plane from equation 35. The dashed line is the intersection of these two planes, and it shows the spatial shift of the image point (black dot) as a function of time lag. The solid line is the intersection of the plane indicated by the red frame and the vertical plane (black frame). Note that this solid line is slightly curved.

Figure 13a shows the vertical image gathers at several locations in space. Note that the shape of the event in the extended image in each panel agrees with the analytical solution shown in Figure 12b. The angle gathers computed using a slant stack along the vertical direction and a slant stack along the 3D surface are shown in Figure 13b and 13c, respectively. Again, we obtain more focused angle gathers using the surface slant stack.

Space-lag CIG

For space-lag extended images (λCIGs), we set $\tau = 0$ in equations 18 and 19 to obtain the system of equations:

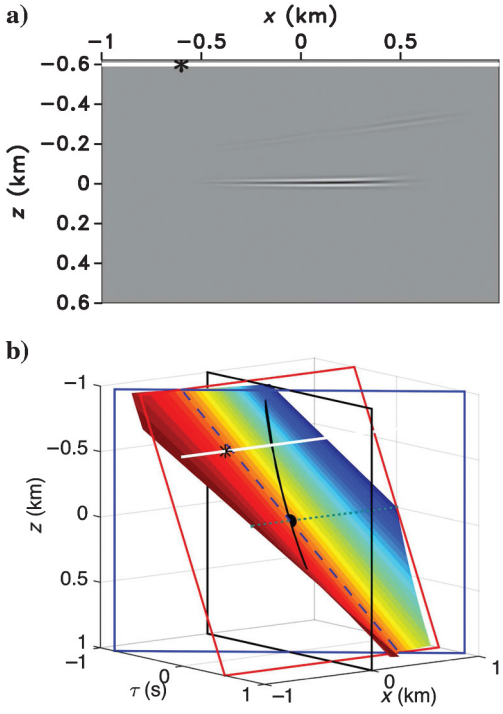


Figure 12. (a) The PS image computed from one shot gather. The reflector is horizontal at $z = 0.0$ km. (b) Predicted spatial shift of a horizontal reflector for $\gamma = 1.8$. The star at coordinates $x = -0.6$ km, $z = -0.6$ km, and $\tau = 0$ s represents the source location, and the white line at $z = -0.6$ km and $\tau = 0$ s represents the receiver locations. The dotted line at $z = 0.0$ km and $\tau = 0$ s shows the zero-lag image. The dashed line illustrates the spatial shift for the image point at (0.0, 0.0) km. The solid line illustrates the extended image for a time-lag gather at a fixed horizontal position ($x = 0.0$ km). Note that these two lines do not overlay. The colors on the surface indicate the contour of the spatial shifts for different image points.

$$\begin{cases} \left(\dfrac{\mathbf{n}_s}{v_s}-\dfrac{\mathbf{n}_r}{v_r}\right)\cdot(\mathbf{x}-\mathbf{x}_o)=\left(\dfrac{\mathbf{n}_s}{v_s}+\dfrac{\mathbf{n}_r}{v_r}\right)\cdot\boldsymbol{\lambda}, & (39)\\ \left(\dfrac{\mathbf{n}_s}{v_s}+\dfrac{\mathbf{n}_r}{v_r}\right)\cdot(\mathbf{x}-\mathbf{x}_o)=\left(\dfrac{\mathbf{n}_s}{v_s}-\dfrac{\mathbf{n}_r}{v_r}\right)\cdot\boldsymbol{\lambda}, & (40)\end{cases}$$

which describes the relation between image shifts $(\mathbf{x}-\mathbf{x}_o)$ and space lag $\boldsymbol{\lambda}$.

Substituting equations 24 and 25 in equations 39 and 40, we obtain

$$\begin{cases} \dfrac{\gamma^2+1+2\gamma\cos 2\theta}{2\gamma}\mathbf{n}\cdot(\mathbf{x}-\mathbf{x}_o)+\sin 2\theta\mathbf{q}\cdot\boldsymbol{\lambda}=\dfrac{1-\gamma^2}{2\gamma}\mathbf{n}\cdot\boldsymbol{\lambda}, & (41)\\ \dfrac{\gamma^2+1+2\gamma\cos 2\theta}{2\gamma}\mathbf{n}\cdot\boldsymbol{\lambda}+\sin 2\theta\mathbf{q}\cdot(\mathbf{x}-\mathbf{x}_o)=\dfrac{1-\gamma^2}{2\gamma}\mathbf{n}\cdot(\mathbf{x}-\mathbf{x}_o). & (42)\end{cases}$$

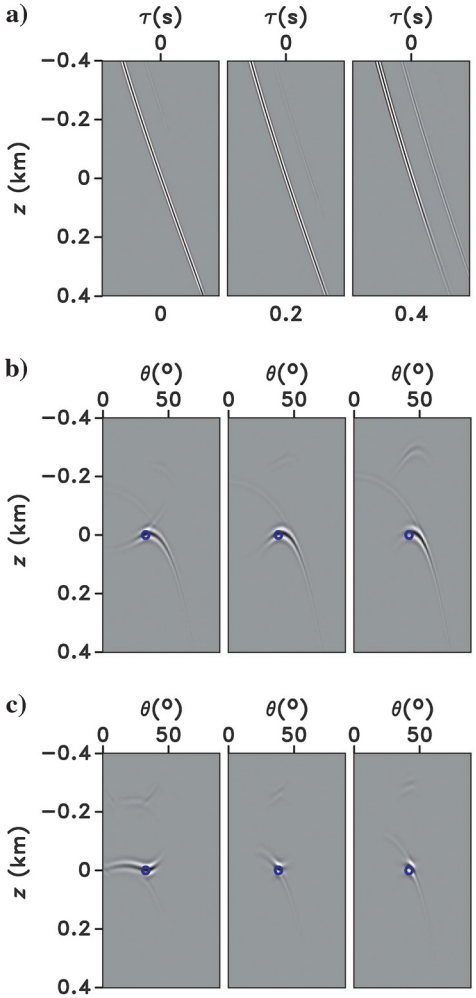


Figure 13. (a) Computed extended image gathers at several x-locations, indicated by the number below each image. The shape of image in each panel matches the corresponding vertical slice of the surface plot in Figure 12b. Computed angles for all samples on the reflector by applying (b) a slant stack along the vertical trace and (c) the method described in Algorithm 1, which applies a slant stack along the surface shown in Figure 12b. The circles represent the analytical solution of the opening angles using the acquisition geometry. The angle gathers in (c) are more focused than those in (b), and they have higher resolutions at larger opening angles.

The terms $\mathbf{n}\cdot(\mathbf{x}-\mathbf{x}_o)$ and $\mathbf{q}\cdot(\mathbf{x}-\mathbf{x}_o)$ are projections of vector $(\mathbf{x}-\mathbf{x}_o)$ onto the normal vector $\mathbf{n}$ and azimuth vector $\mathbf{q}$, respectively.

We compute a 3D PS angle gather for the 3D model shown in Figure 3 using the $\boldsymbol{\lambda}$CIG (Figure 14). The input $\boldsymbol{\lambda}$CIG is 6D, as a function of space $\mathbf{x}$ and $\boldsymbol{\lambda}$, and Figure 14 shows the $\boldsymbol{\lambda}$CIG at $x=0.2$ km, $y=0.2$ km, and $\lambda_z=0$ km. By using Algorithm 1, we obtain a well-focused PS angle gather that matches the analytical solution.

Equations 41 and 42 simplify in the acoustic case for which velocity the ratio $\gamma=1$:

$$\begin{cases} \mathbf{n}\cdot(\mathbf{x}-\mathbf{x}_o)+\tan\theta(\mathbf{q}\cdot\boldsymbol{\lambda})=0, & (43)\\ \tan\theta[\mathbf{q}\cdot(\mathbf{x}-\mathbf{x}_o)]+(\mathbf{n}\cdot\boldsymbol{\lambda})=0. & (44)\end{cases}$$

Note that equation 43 is similar to the equation proposed by Sava and Fomel (2003). For PP reflections, if the space lag is parallel to the normal vector $\mathbf{n}$, the image shift $(\mathbf{x}-\mathbf{x}_o)$ lies in the local interface plane. If the space-lag is orthogonal to the normal vector $\mathbf{n}$, the image shift $(\mathbf{x}-\mathbf{x}_o)$ is parallel to the normal vector $\mathbf{n}$.

EXAMPLE

SEG/EAGE example

We show angle gathers computed using the proposed elastic angle-decomposition methodologies for the synthetic SEG/EAGE salt model (Aminzadeh et al., 1996), shown in Figure 15a. We add a horizontal reflector at $z=0.3$ km, and we compute the half-opening and azimuth angles for an image point on the horizontal reflector at location (0.3, 0.4, 0.3) km. The acquisition geometry consists of 99 sources (the black dots in Figure 15a) and a 2D network of receivers at $z=0.02$ km. We generate 3C shot gathers using a vertical displacement source with a 100 Hz peak frequency Ricker wavelet.

As shown in Figure 15b, due to the existence of the salt body above the horizontal reflector, it is difficult to illuminate the considered image point at location (0.3, 0.4, 0.3) km from certain azimuths. Figures 16 and 17 show the stacked angle gather at location (0.3, 0.4, 0.3) km, computed from PP and PS CIP gathers, respectively, using Algorithm 1. Both angle gathers show similar illumination patterns. If we define azimuth $\phi=0^\circ$ as east, for the PP

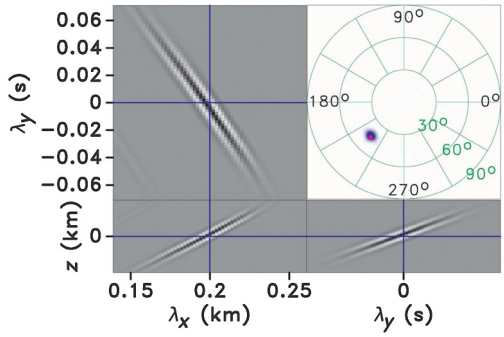


Figure 14. The PS $\boldsymbol{\lambda}$CIG at $x=0.2$ km, $y=0.2$ km, and the wide-azimuth angle gather of a picked image point at coordinates (0.2, 0.2, 0.2) km for the 3D model shown in Figure 3. The red dot represents the analytical solution of the opening and azimuth angle using the acquisition geometry.

Downloaded 10/27/17 to 138.67.129.100. Redistribution subject to SEG license or copyright; see Terms of Use at http://library.seg.org/

image, we observe that this image point is mainly illuminated from the west, and for the PS image, the image point is illuminated mostly from the southwest. As expected, the illumination of PP and PS angle gathers is heavily impacted by the presence of the salt body to the east.

North Sea data example

Finally, we show an example from Volve field, which is located in the Norwegian North Sea and is characterized by a complex subchalk reservoir (Szydlik et al., 2007). The acquisition geometry consists of 12 parallel OBC receiver lines, and each line contains 240 receivers. The provided PP data were preprocessed for PP imaging, whereas the PS data were preprocessed for PS imaging. The PP data contain mainly upgoing PP reflections computed from the hydrophone and vertical geophone components using PZ summation (Hoffe et al., 1999). The PS data set was obtained by rotating the horizontal inline and crossline geophone components onto the source-receiver (radial) direction (Gaiser, 1999). We bandpass both data sets to 0–15 Hz to allow for wavefield simulation on a relatively coarse grid, thereby reducing computational cost. We subsample the receivers and use 142 receivers gathers to compute PP and PS images. The x- and y-spacing of the receivers are 400 and 500 m, respectively. Each receiver gather consists of approximately 1000 traces.

We compute the PP and PS images above the chalk layer using the PP and PS imaging conditions (equations 1 and 2), respectively. Note that the reflector normal vector $\mathbf{n}$ from the PP image is almost vertical above the chalk layer throughout this field. Figure 18a shows the stacked PP image for 140 receiver gathers, and Figure 18b shows the stacked PS image. Because the wavelength of the S-wave is typically shorter than that of the P-wave, the PS image tends to have higher resolution than the PP image. However, the PS data have a lower signal-to-noise ratio than the PP data, and reflectors in the PS image are less continuous than those in the PP image.

We compute extended CIP gathers at the depth of 2.1 km for four receiver gathers, whose locations are indicated by the stars in Figure 18a and 18b. The maximum x- and y-offsets of the four receiver gathers are 5 and 1.4 km, respectively. Figure 19a–19d shows the PP extended CIP gathers and angle gathers for these receiver gathers, and Figure 20a–20d shows the PS extended CIP gathers and angle gathers. The PS CIP and angle gathers are noisier than the PP gathers. The angle gathers show that this image point is illuminated from various directions.

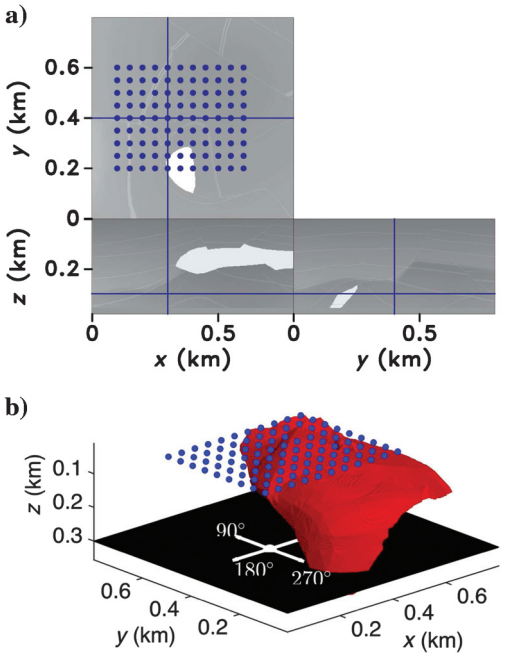


Figure 15. (a) The SEG/EAGE model. The dots show the source locations. (b) Relative position of the image point at location (0.3, 0.4, 0.3) km and the salt body.

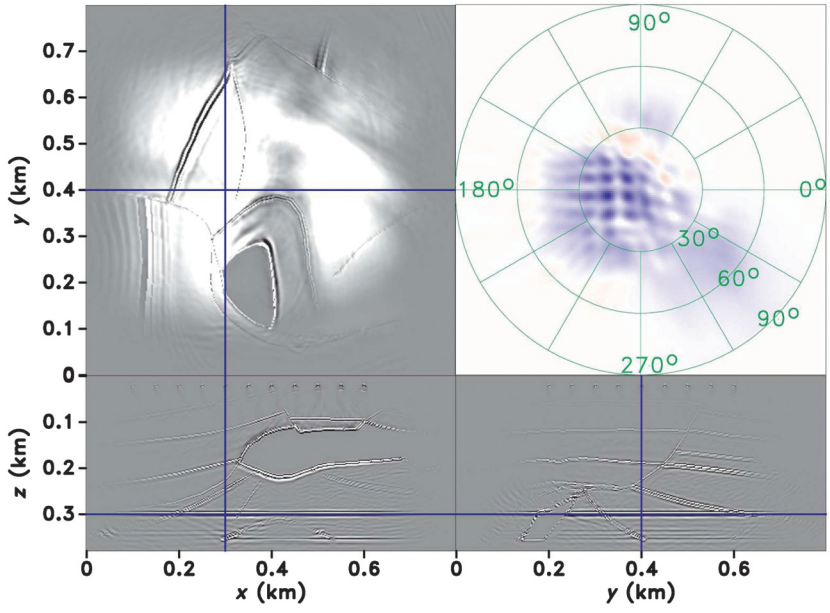


Figure 16. The PP image and angle gathers at location (0.3, 0.4, 0.3) km, computed using the extended PP image. We define azimuth $\phi = 0^{\circ}$ in the definition pointing east. This image point is mainly illuminated from the west direction.

Downloaded 10/27/17 to 138.67.129.100. Redistribution subject to SEG license or copyright; see Terms of Use at http://library.seg.org/

DISCUSSION

Elastic 3D angle gathers can be computed from time-lag or space-lag CIG, as well as from mixed time- and space-lag CIP gathers. The three algorithms we propose in the paper are derived from the same system of equations, and they compute angle gathers using different extended gathers. The first algorithm uses combined time- and space-lag CIP gathers to compute angles for individual image points, the second algorithm uses time-lag CIGs to map all points simultaneously from the model space to the angle domain, and the

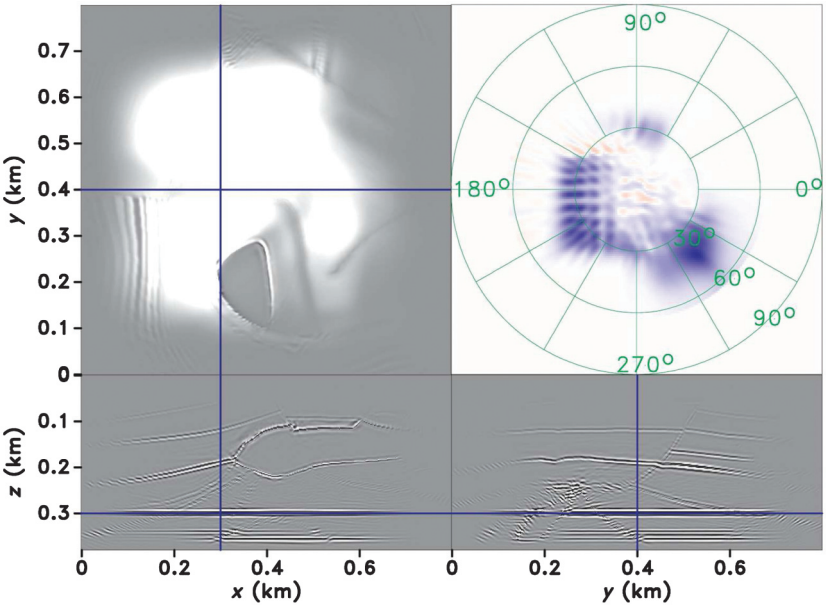


Figure 17. The PS image and angle gathers at location (0.3, 0.4, 0.3) km, computed using the extended PS image. We define azimuth $\phi = 0^{\circ}$ as east. This image point is illuminated from the west and the south directions.

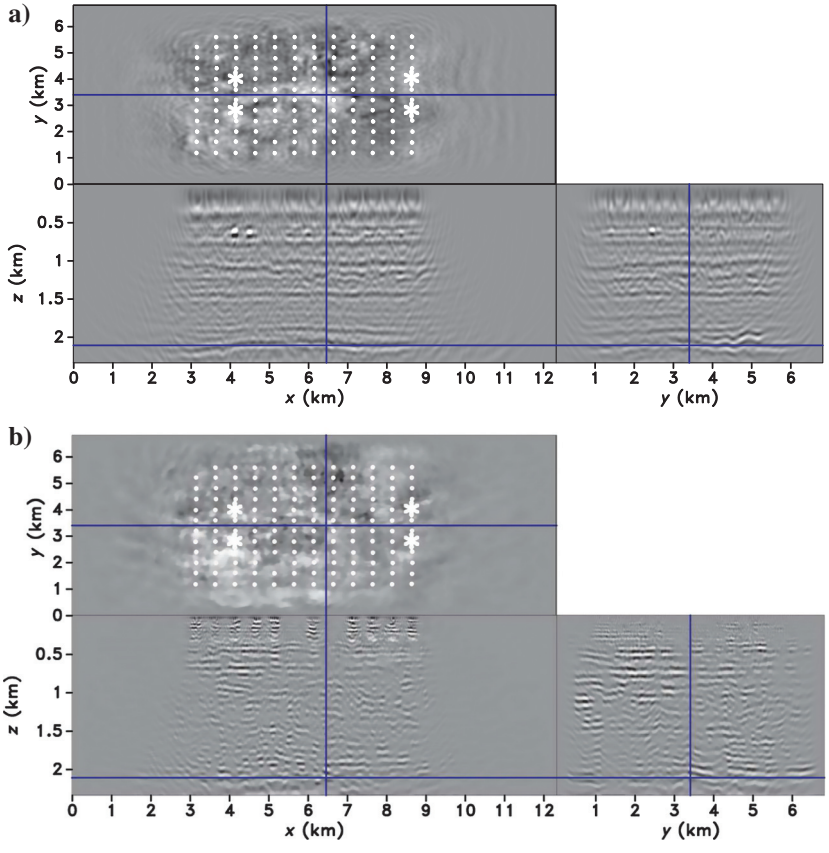


Figure 18. Volve data example. (a) The PP and (b) PS images computed using 142 receiver gathers. The dots show locations of all the receivers, and the stars highlight four receiver gathers that are used for angle decomposition. The reflectors in the PS image are less continuous than those in the PP image.

Downloaded 10/27/17 to 138.67.129.100. Redistribution subject to SEG license or copyright; see Terms of Use at http://library.seg.org/

Downloaded 10/27/17 to 138.67.129.100. Redistribution subject to SEG license or copyright; see Terms of Use at http://library.seg.org/

third algorithm uses space-lag CIGs to compute angle gathers for all image points in the model space. Depending on the application, we may select an algorithm based on its computational cost as well as the desired image resolution. When we compute angle gathers for a subset of image points, the first algorithm is the most computationally efficient because it requires extended images at only the chosen image locations. If we are to compute angle gathers for all points in the image domain, the first algorithm is the most expensive, and the second algorithm using time-lag CIGs is the most efficient in terms of computational cost. However, because the azimuthal resolution of angle gathers computed from time-lag CIGs is limited, we should use the third algorithm for high-resolution azimuthal information.

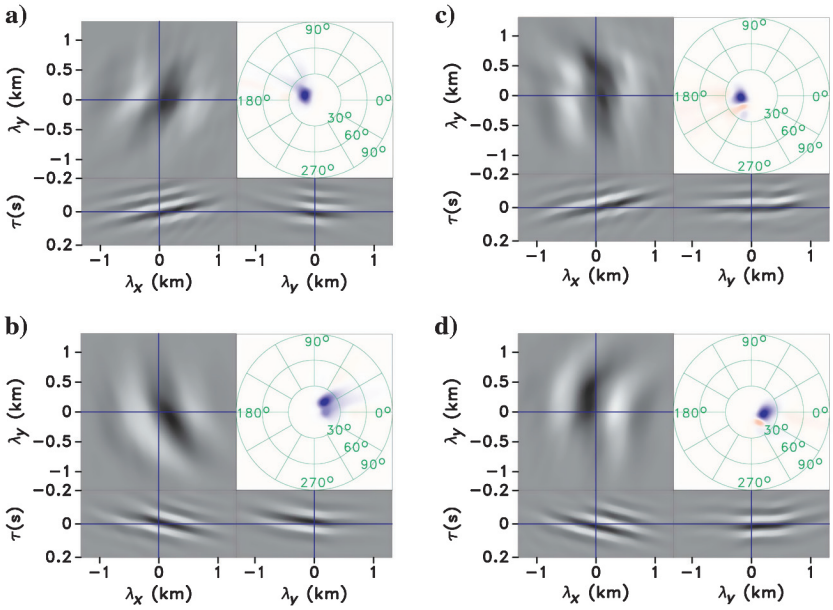


Figure 19. The PP extended CIP and wide-azimuth angle gathers for four receiver gathers. The receivers are at (a) (4.1, 4.0, 0.1), (b) (8.6, 4.0, 0.1), (c) (4.1, 2.8, 0.1), and (d) (8.6, 2.8, 0.1) km. The angle gathers show that this image point is illuminated by the four receivers from various directions with PP reflections.

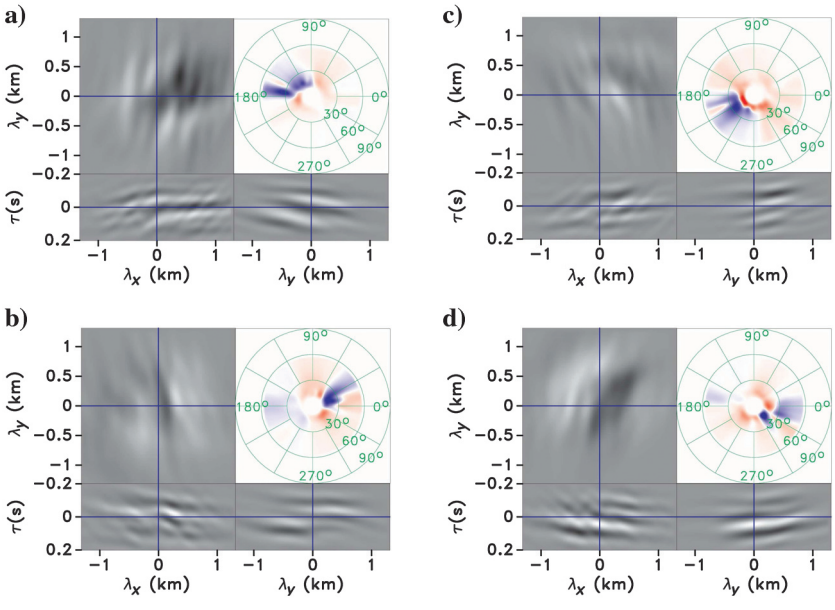


Figure 20. The PS extended CIP and wide-azimuth angle gathers for four receiver gathers. The receivers are at (a) (4.1, 4.0, 0.1), (b) (8.6, 4.0, 0.1), (c) (4.1, 2.8, 0.1), and (d) (8.6, 2.8, 0.1) km. The angle gathers show that this image point is illuminated by the four receivers from various directions with PS reflections.

CONCLUSION

We propose extended imaging conditions to compute scalar PP, PS, SP, and SS images, and develop three methods to compute opening and azimuth angle gathers. The first method uses combined time- and space-lag CIP gathers to compute angle gathers, and the other two methods use either time-lag or space-lag CIG to map all image points simultaneously from the model space to the angle domain. Examples in 2D and 3D demonstrate that our methods correctly handle dipping reflectors as well as converted wave images. The computed angle gathers correctly produce the illumination pattern for subsurface image points, which is important for acquisition design, model building, and reservoir characterization.

ACKNOWLEDGMENTS

We thank the sponsors of the Center for Wave Phenomena, whose support made this research possible. We also thank Statoil ASA and the Volve license partners ExxonMobil E & P Norway AS and Bayerngas Norge AS, for the release of the Volve data. The views expressed in this paper are of the authors and do not necessarily reflect the views of Statoil ASA and the Volve field license partners. The reproducible numeric examples in this paper use the Madagascar open-source software package (Fomel et al., 2013) freely available from http://www.ahay.org.

REFERENCES

Aminzadeh, F., N. Burkhard, J. Long, T. Kunz, and P. Duclos, 1996, Three dimensional SEG/EAEG models: An update: The Leading Edge, **15**, 131–134, doi: 10.1190/1.1437283.

Audebert, F., P. Froidevaux, I. Huard, L. Nicoletis, and J. Svay-Lucas, 2000, A multi-angle toolbox for restored amplitude images and AVA-gathers: 70th Annual International Meeting, SEG, Expanded Abstracts, 1020–1023.

Balch, A. H., and C. Erdemir, 1994, Sign-change correction for prestack migration of P-S converted wave reflections: Geophysical Prospecting, **42**, 637–663, doi: 10.1111/j.1365-2478.1994.tb00233.x.

Biondi, B., and W. W. Symes, 2004, Angle-domain common-image gathers for migration velocity analysis by wavefield-continuation imaging: Geophysics, **69**, 1283–1298, doi: 10.1190/1.1801945.

Brandsberg-Dahl, S., M. V. de Hoop, and B. Ursin, 1999, Velocity analysis in the common scattering-angle/azimuth domain: 68th Annual International Meeting, SEG, Expanded Abstracts, 1715–1718.

De Bruin, C., C. Wapenaar, and A. Berkhout, 1990, Angle-dependent reflectivity by means of prestack migration: Geophysics, **55**, 1223–1234, doi: 10.1190/1.1442938.

Dellinger, J., and J. Etgen, 1990, Wave-field separation in two-dimensional anisotropic media: Geophysics, **55**, 914–919, doi: 10.1190/1.1442906.

Duan, Y., and P. Sava, 2014, Elastic reverse-time migration with OBS multiples: 84th Annual International Meeting, SEG, Expanded Abstracts, 4071–4076.

Duan, Y., and P. Sava, 2015a, Robustness of the scalar elastic imaging condition for converted waves: CWP Research Report, 41–48.

Duan, Y., and P. Sava, 2015b, Scalar imaging condition for elastic reverse time migration: Geophysics, **80**, no. 4, S127–S136, doi: 10.1190/geo2014-0453.1.

Etgen, J. T., 1988, Prestacked migration of P and SV-waves: 58th Annual International Meeting, SEG, Expanded Abstracts, 972–975.

Fomel, S., P. Sava, I. Vlad, Y. Liu, and V. Bashkardin, 2013, Madagascar: Open-source software project for multidimensional data analysis and reproducible computational experiments: Journal of Open Research Software, **1**, e8, doi: 10.5334/jors.ag.

Frigerio, J. O., and P. C. Sava, 2011, Angle-azimuth decomposition of converted waves using extended images: Presented at the 12th International Congress of the Brazilian Geophysical Society.

Gaiser, J., 1999, Applications for vector coordinate systems of 3-D converted-wave data: The Leading Edge, **18**, 1290–1300, doi: 10.1190/1.1438202.

Hoffe, B. H., H. C. Bland, G. F. Margrave, P. M. Manning, and D. S. Foltinek, 1999, Analysis of the effectiveness of 3-C receiver arrays for converted wave imaging: 69th Annual International Meeting, SEG, Expanded Abstracts, 649–652.

Patrikeeva, N., and P. Sava, 2013, Comparison of angle decomposition methods for wave-equation migration: 83rd Annual International Meeting, SEG, Expanded Abstracts, 3773–3778.

Rickett, J. E., and P. C. Sava, 2002, Offset and angle-domain common image-point gathers for shot-profile migration: Geophysics, **67**, 883–889, doi: 10.1190/1.1484531.

Sava, P., 2007, Stereographic imaging condition for wave-equation migration: Geophysics, **72**, no. 6, A87–A91, doi: 10.1190/1.2781582.

Sava, P., and B. Biondi, 2004, Wave-equation migration velocity analysis. I: Theory: Geophysical Prospecting, **52**, 593–606, doi: 10.1111/j.1365-2478.2004.00447.x.

Sava, P., and S. Fomel, 2006, Time-shift imaging condition in seismic migration: Geophysics, **71**, no. 6, S209–S217, doi: 10.1190/1.2338824.

Sava, P., and I. Vlad, 2011, Wide-azimuth angle gathers for wave-equation migration: Geophysics, **76**, no. 3, S131–S141, doi: 10.1190/1.3560519.

Sava, P. C., and S. Fomel, 2003, Angle-domain common-image gathers by wavefield continuation methods: Geophysics, **68**, 1065–1074, doi: 10.1190/1.1581078.

Symes, W. W., 1993, A differential semblance criterion for inversion of multioffset seismic reflection data: Journal of Geophysical Research: Solid Earth, **98**, 2061–2073.

Szydlik, T., P. Smith, S. Way, L. Aamodt, and C. Friedrich, 2007, 3D PP/PS prestack depth migration on the Volve field: First Break, **25**, 43–47.

Vyas, M., X. Du, E. Mobley, and R. Fletcher, 2011, Methods for computing angle gathers using RTM: 73rd Annual International Conference and Exhibition, EAGE, Extended Abstracts, doi: 10.3997/2214-4609.20149175.

Xie, X.-B., and R.-S. Wu, 2002, Extracting angle domain information from migrated wavefield: 72nd Annual International Meeting, SEG, Expanded Abstracts, 1360–1363.

Xu, S., H. Chauris, G. Lambaré, and M. Noble, 2001, Common-angle migration: A strategy for imaging complex media: Geophysics, **66**, 1877–1894, doi: 10.1190/1.1487131.

Xu, S., Y. Zhang, and B. Tang, 2011, 3D angle gathers from reverse time migration: Geophysics, **76**, no. 2, S77–S92, doi: 10.1190/1.3536527.

Yan, J., and W. Ross, 2013, Improving the stability of angle gather computation using Poynting vectors: 83rd Annual International Meeting, SEG, Expanded Abstracts, 3784–3788.

Yan, J., and P. Sava, 2008, Isotropic angle-domain elastic reverse-time migration: Geophysics, **73**, no. 6, S229–S239, doi: 10.1190/1.2981241.

Yan, R., and X.-B. Xie, 2012, An angle-domain imaging condition for elastic reverse time migration and its application to angle gather extraction: Geophysics, **77**, no. 5, S105–S115, doi: 10.1190/geo2011-0455.1.

Yang, T., and P. Sava, 2015, Image-domain wavefield tomography with extended common-image-point gathers: Geophysical Prospecting, **63**, 1086–1096, doi: 10.1111/1365-2478.12204.

Yoon, K., and K. J. Marfurt, 2006, Reverse-time migration using the Poynting vector: Exploration Geophysics, **37**, 102–107, doi: 10.1071/EG06102.

Yoon, K., K. J. Marfurt, and W. Starr, 2004, Challenges in reverse-time migration: 74th Annual International Meeting, SEG, Expanded Abstracts, 1057–1060.

Zhang, Y., and J. Sun, 2008, Practical issues of reverse time migration-true-amplitude gathers, noise removal and harmonic-source encoding: 70th Annual International Conference and Exhibition, EAGE, Extended Abstracts, doi: 10.3997/2214-4609.20147708.

Downloaded 10/27/17 to 138.67.129.100. Redistribution subject to SEG license or copyright; see Terms of Use at http://library.seg.org/